Numerical Simulations of a Traveling Plane-Wave Actuator for Microfluidic Applications

A.F. Tabak and S. Yesilyurt[*]
Sabanci University, Istanbul, Turkey

*Corresponding author: Sabanci University, Tuzla, Istanbul, 34956, Turkey, syesilyurt@sabanciuniv.edu

Abstract: Continuous forming and propagation of large planar deformations on a thin solid elastic film can create propulsion when the film is immersed in a fluid. Microscopic organisms such as spermatozoa use similar mechanisms to propel themselves. In this work, we present a numerical analysis of the effect of traveling plane-wave deformations on an elastic-film actuator within a fluid medium inside a channel. In particular, we analyzed a micropump that consists of a wave actuator, which is placed in a channel to pump the fluid in the direction of the plane-deformation waves. The unsteady flow over the moving boundary between the parallel plates has very low Reynolds number, and, hence, is modeled using the two-dimensional time-dependent Stokes equations. The fluid-structure interaction due to moving boundary is modeled with the arbitrary Lagrangian Eulerian (ALE) method incorporating the Winslow smoothing. COMSOL is used to solve two-dimensional time-dependent Stokes equations on a deforming mesh, and to carry out simulations of the flow. Effects of the deformation amplitude, wavelength, frequency and channel height on the flow rate are presented.

Keywords: Micropump, deforming mesh, traveling-wave actuator.

1. Introduction

Microfluidic components such as micropumps are of particular interest for medical, biotechnology, and environmental sensor applications such as drug delivery, sensor measurements and DNA replication [1-4]. Reciprocating positive displacement pumps are used to move the fluid mechanically in the sense that a structural component, which is, usually a membrane, does work on the fluid [4]. Reciprocating pumps consist of a diaphragm membrane, or a piston, and at least one or two check valves and similar components that direct the flow [5,6]. Although large flow rates are obtained with displacement pumps, application of large voltages is necessary to actuate piezoelectric-material drivers [7,8], in addition to the complexity of the design and unsteady flow rates [9]. Producing controllable steady flows with mechanical micropumps remains a challenge.

Propulsion mechanisms of microscopic organisms can be a viable option for pumping of fluids in microchannels. Micro organisms such as spermatozoa and bacteria use their flagella to propel themselves [10,11]. Bacterial flagella are usually helically shaped, and driven by a rotary engine at the base that creates a screw-like motion. Flagella of spermatozoa and other eukaryotic cells resemble to elastic rods, whose stress-induced, sudden bending deformations propagate towards the tip similar to a beating motion [12]. In principle, the mechanism that leads to the propulsion of the micro organism can be used to pump the fluid inside a channel comprising of an actuator thin-film, on which the deformation waves are formed and propagated.

Here, we model and present simulations of the flow due to traveling-wave deformations on a solid thin-film immersed in a fluid inside a channel as shown in figure 1. Effects of the amplitude, frequency, channel height and wavelength on the flow rate are quantified and manifested through a number of simulations.
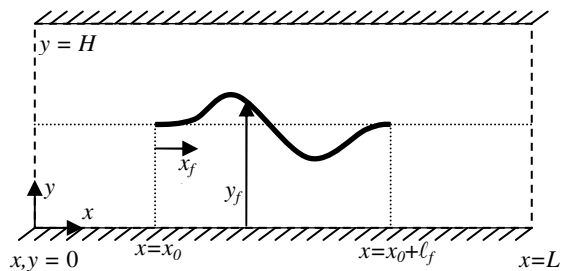

Figure 1. Layout of the channel that contains a solid film on which traveling-wave deformations

2. Governing equations

The vertical motion of the thin film, y_f, as a function of time, t, and position on the film, x_f, is specified as a traveling wave in the x–direction:

$$y_f\left(x_f,t\right)= B\left(x_f,t\right)\sin\left(\omega t - 2\pi x_f/\lambda\right) \quad (1)$$

Here, ω is the angular frequency, λ is the wavelength, and $B(x_f,t)$ is the amplitude shape function, which is given by:

$$B\left(x_f,t\right)= 4B_0\left(1-\frac{x_f}{\ell_f}\right)\left(\frac{x_f}{\ell_f}\right)\min\left(t,\frac{1}{f}\right) \quad (2)$$

where ℓ_f is the length of the film, and f is the frequency. The amplitude shape function in (2) is a parabolic envelope that confines the deformation waves, and consists of a ramp function in time that ensures the simulations to start from initial conditions at rest.

Flow induced by the motion of the boundary according to (1) and (2) is governed by the Stokes equations due to low Reynolds number of the flow in the channel. Namely, we have:

$$\rho\left(\frac{\partial \mathbf{U}}{\partial t}+\mathbf{u}_m\cdot\nabla\mathbf{U}\right)=-\nabla p+\mu\nabla^2\mathbf{U} \text{ in } \Omega(t), \quad (3)$$

and

$$\nabla\cdot\mathbf{U}=0 \quad \text{in} \quad \Omega(t). \quad (4)$$

In (3), $\mathbf{U}=[u,v]'$ is the velocity vector, p is the pressure, ρ is fluid's density, and μ is the dynamic viscosity of the fluid. The time-dependent domain, $\Omega(t)$, corresponds to the volume occupied by the fluid at time t, and bounded by fixed boundaries that correspond to the channel's walls, inlet and outlet, and moving boundaries that coincide with the thin-film actuator's surface. The $\mathbf{u}_m$ in (3) represents the velocity of the deforming domain $\Omega(t)$.

No-slip boundary conditions are specified on the plate walls for Stokes equations:

$$u\left(x,0,t\right)= u\left(x,H,t\right)= 0$$
$$v\left(x,0,t\right)= v\left(x,H,t\right)= 0. \quad (5)$$

Slip conditions are specified on moving boundaries of the actuator film:

$$u\left(x_f,y_f,t\right)=0 \quad (6)$$

and after the initial ramp,

$$v\left(x_f,y_f,t\right)=\frac{dy_f}{dt} \quad (7)$$
$$= \omega B\left(x,t\right)\cos\left(\omega t - kx_f\right).$$

At the channel inlet and outlet, unless otherwise noted, we use the neutral flow boundary conditions [13], which correspond to vanishing total forces acting in the normal direction on the surface:

$$\left[-p\mathbf{I}+\boldsymbol{\tau}\right]\cdot\mathbf{n}\big|_{x=\{0,L\},y,t}=\mathbf{0} \quad (8)$$

where $\mathbf{n}$ is the outward normal of the surface, and $\boldsymbol{\tau}$ is the viscous stress tensor [14].

The initial condition for (3) is the flow at rest, i.e. the velocity components and the pressure are all equal to zero at $t=0$:

$$u\left(x,y,0\right)= v\left(x,y,0\right)= p\left(x,y,0\right)=0. \quad (9)$$

The Stokes equations, (3), subject to incompressibility, (4), boundary, (5), (7), (8), and initial conditions (9) are discretized using triangular Lagrange elements that use quadratic basis functions for the velocity and linear basis for the pressure. Due to the motion of the thin-film actuator boundaries, the arbitrary Lagrangian Eulerian (ALE) method that incorporates Winslow smoothing [13,15,16] is used to obtain the velocity of the deforming mesh on which Stokes equations are solved.

The Laplace equation is solved to calculate the mesh velocity, $\mathbf{u}_m$:

$$\nabla^2\mathbf{u}_m=0 \quad \text{in} \quad \Omega(t) \quad (10)$$

The boundary conditions, which (10) is subject to, are moving boundary conditions on the thin-film, akin to (7), and zero displacement elsewhere. Namely,

$$u_m\left(x_f,y_f,t\right)=0, \quad (11)$$

$$v_m\left(x_f,y_f,t\right)=\frac{dy_f}{dt}, \quad (12)$$

$$\begin{bmatrix}u_m\left(0,y,t\right)\\v_m\left(0,y,t\right)\end{bmatrix}=\begin{bmatrix}u_m\left(L,y,t\right)\\v_m\left(L,y,t\right)\end{bmatrix}=\begin{bmatrix}0\\0\end{bmatrix} \quad (13)$$

and

$$\begin{bmatrix}u_m\left(x,0,t\right)\\v_m\left(x,0,t\right)\end{bmatrix}=\begin{bmatrix}u_m\left(x,H,t\right)\\v_m\left(x,H,t\right)\end{bmatrix}=\begin{bmatrix}0\\0\end{bmatrix}. \quad (14)$$

Having calculated the mesh velocity, $\mathbf{u}_m$, from (10) and subject to (11)-(14), one can find

the updated mesh in $\Omega(t)$ and solve Stokes equations given by (3). The Laplace equation is solved using the same triangulation of the domain as the one used for the solution of Stokes equations. Moreover, quadratic basis functions are used for the mesh velocity components in the finite-element procedure [13].

The instantaneous flow rate per unit depth delivered by the pump for a given set of inputs, $\{H, B_0, f, \lambda\}$, is computed by the integration of the x–component of the velocity over the inlet or outlet of the channel as given by:

$$Q(t) = \int_{y=0}^{H} \mathbf{u}(t) \cdot (\mp\mathbf{n}) dy, \qquad (15)$$

where $\mathbf{n}$ corresponds to inlet or outlet surface normal (outward), due to which the '+' sign applies for the outlet flow, and '–' for the inlet flow. In practice, we also check the conservation of mass by comparing inlet and outlet flow rates, the relative difference of which always remains below the tolerance of the numerical procedure, i.e. $2|Q_{in} - Q_{out}|/|Q_{in} + Q_{out}| \approx 10^{-8} < 10^{-3}$.

The time-averaged flow rate is computed from the integral of the instantaneous flow rate given by (15) over at least 3 full periods of the deformations after a steady-periodic state is observed:

$$\bar{Q} = \frac{1}{(m-n)/f} \int_{n/f}^{m/f} Q(t) dt, \qquad (16)$$

where m and n are integers, and $m > n$. Due to relatively short length of the channel the flow becomes steady-periodic within first two periods, i.e. $n = 2$.

3. Results

Our numerical results are presented in terms of dimensionless quantities, which are scaled by characteristic length, time and velocity and fluid properties; the base case is as shown in table 1. Unless otherwise noted, these scales are used in simulations. Moreover, the default values of dimensionless geometric variables are listed in table 2; where the superscript '*' denotes nondimensional quantities.

For the standard case presented in table 2, approximately 30000 linear equations are solved for each time-step for 5 dimensionless time units

that correspond to 5 full periods. Simulation outputs converge to a steady-periodic state within two periods. To calculate time-averaged quantities, we use last three periods, i.e. $m = 5$, and $n = 2$ in (16). A standard simulation takes about 6 hours on a single processor of a dual 2.4 GHz Xeon workstation with 1GB of RAM.

Table 1. Characteristic scales and their base values used in simulations and comparison of results

Characteristic scales	Representative values
Length, ℓ_0	2.5×10^{-4} m
Velocity, U_0	5×10^{-4} m/s
Time, t_0	0.5 s
Pressure, p_0	ρU_0^2, 2.5×10^{-4} Pa for water

Table 2. Default values for geometric variables used in simulations, unless otherwise noted

Geometric variables (dimensionless)	Value
Channel height, H^*	2.5
Channel length, L^*	9.0
Film's length, ℓ_f^*	5.0
Maximum amplitude of the deformation, B_0^*	0.0581
Wavelength, λ^*	5.0
Wave speed, c^*	5.0

In figure 2, the relationship between the average velocity of the flow, $\bar{U}^* = \bar{Q}^*/H^*$, and channel-height to amplitude ratio is shown. As H/B_0 ratio approaches to 2, which is the case when the film touches to channel walls, the pump works as a displacement pump, and, expectedly, provides the largest velocity. According to the figure, average velocity inversely scales with the square of the H/B_0 ratio, i.e.

$$\bar{U} \approx \frac{a}{b + (H/B_0)^2}$$
(17)

where a and b are positive constants. This result, in fact, agrees with the asymptotic analysis of the propulsion of micro organisms near solid boundaries by Katz [17] for amplitudes on the order of channel half-height.

In figure 3, the dimensionless average flow rate is plotted against the dimensionless fre-

quency. It is clear that the flow rate increases linearly with the frequency. This result agrees well with the asymptotic analyses of the propulsion of micro organisms by Taylor [18] in an infinite fluid medium, and by Katz [17] between parallel plates when the amplitude is small compared to the separation between the channel walls. Both Katz [17] and Taylor [18] concluded that the average speed must be proportional to the wave speed, which is the frequency for constant wavelength, in their asymptotic analyses.

Figure 2. Variation of the nondimensional average velocity with the channel height to maximum amplitude ratio.
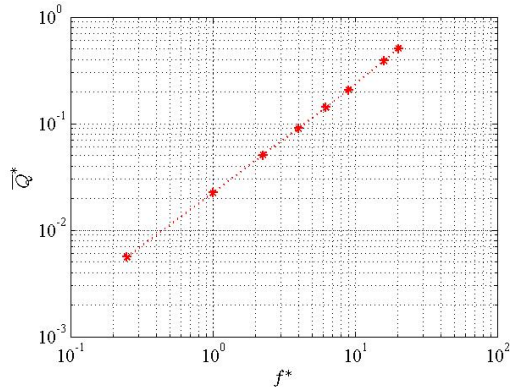

Figure 3. Variation of the nondimensional flow rate with the nondimensional frequency.

The role of wavelength in our finite-length film is very important, and despite the monotonic increase of the flow rate with the wavelength, the relationship between the two is not linear as suggested by analytical (asymptotical) studies of both Taylor [18] and Katz [17].

In figure 4, the relationship between the flow rate and the wavelength is shown. It is clear that increasing the wavelength results in increasing flow rate. However one would expect to have zero net flow rates, if the wavelength becomes much larger than the length of the film –as the vertical motion of the film without the wave propagation would simply stir the fluid and not yield any net flow. Furthermore, there are two distinct regimes that govern the flow and vary with the wavelength to film's length ratio, λ/ℓ_f. The first regime is observed when $\lambda/\ell_f \ll 1$, for which there is somewhat steady flow in the channel that remains always positive. The second regime is observed when the wavelength is comparable to the size of the film, i.e. $\lambda/\ell_f \sim 1$, for which another flow regime emerges in the channel resulting in an unsteady flow rate that becomes even negative in certain portions of a full period. Snapshots of the pressure distribution with streamlines for the first case, and velocity arrows for the second case are shown in figures 5 and 6 respectively.
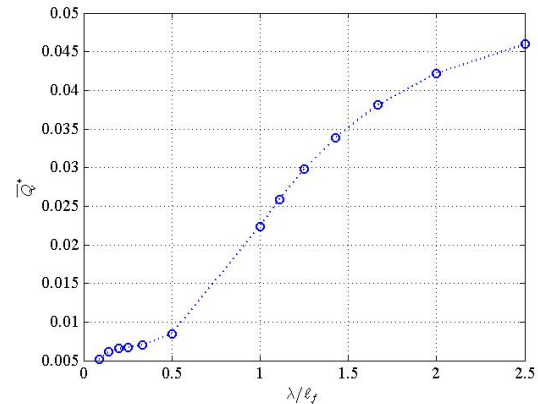

Figure 4. Variation of the nondimensional flowrate with the wavelength to film length ratio. (Only the wavelength is varied.)

When the wavelength is small compared to the length of the film (figure 5), two stationary recirculations remain in the middle of the channel above and below the film. That corresponds to a steady pressure distribution along the channel that resembles to the distribution for a converging-diverging nozzle with a pressure source in the middle. Moreover, from different snapshots at different times, and from the time-

dependent flow rate given by (15), we observed that streamlines exhibit near steady flow at the inlet and exit of the channel.

On the other hand, when the wavelength is comparable to the size of the film (figure 6), pressure zones brought about by the motion of the film extend to the channel walls, and travel downstream with the propagation of the wave. This results in an unsteady flow that even becomes negative sometimes. This regime clearly is not desirable if one wishes to keep a steady flow in his application. However, according to figure 4, it is clear that one will attain higher average flow rates as the wavelength increases.
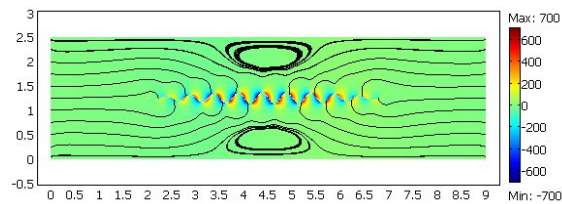

Figure 5. Pressure distribution (color shading), and streamlines for $t^* = 5$, and $\lambda/\ell_f = 0.1$.
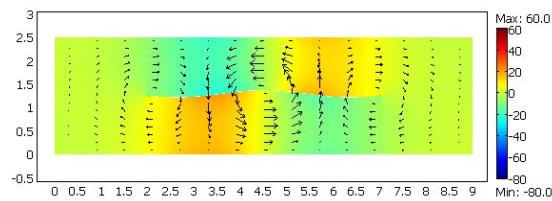

Figure 6. Pressure distribution (color shading), and velocity vectors (arrows scaled with the magnitude) for $t^* = 4.15$, and $\lambda/\ell_f = 1$.

4. Conclusions

A dynamic pumping mechanism that can be used for micro flows is demonstrated by means of numerical simulations. The propulsion effect of the traveling-wave deformations on a thin solid film immersed in a fluid in a channel is modeled with Stokes equations and solved on a deforming mesh due to the motion of the boundary with the ALE method. Parametric dependence of the flow rate on the ratio of the deformation amplitude to the channel height, frequency and wavelength is obtained by means of a number of numerical simulations. The relative effect of the amplitude-to-channel-height ratio and the frequency (wave speed for constant wavelength)

is found to be in accordance with the former asymptotic analytical results for the infinite-film.

Due to the finite-length case we studied here, the wavelength has a profound effect on the flow rate as two different flow regimes emerge for very small wavelengths compared to the film's length and the ones comparable to the length of the film. For small wavelengths, almost steady positive flow is observed at all times. For large wavelengths, flow rate oscillates with a large magnitude resulting in negative values during some periods. A detailed analysis of the flow and a characterization of a typical pump are presented elsewhere [19].

5. References

1. D. L. Polla, A. G. Erdman, W. P. Robbins, D. T. Markus, J. Diaz-Diaz, R. Rizq, Y. Nam, H. T. Bricker, A. Wang, and P. Krulevitch, "Microdevices in Medicine," *Annu. Rev. Biomed. Eng.*, **2**, 551-76 (2000)
2. J.G.E. Gardeniers, and A. van den Berg, "Lab-on-a-chip systems for biomedical and environmental monitoring," *Anal. Bioanal. Chem.*, **378**, 1700-1703 (2004)
3. C.F. Lin, G.B. Lee, C.H. Wang, H.H. Lee, W.Y. Liao, and T.C. Chou, "Microfluidic pH-sensing chips integrated with pneumatic fluid-control devices', *Biosens. Bioelectron.*, **21**, 419–425 (2005)
4. D.J. Laser and J.G. Santiago, "A review of micropumps," *J. Micromech. Microeng.*, **14**, R35-R64 (2004)
5. H.T.G. Van Lintel, F.C.M. Van de Pol, and S. Bouwstra, "A piezoelectric micropump based on micromachining of silicon," *Sensors and Actuators*, **15**, 153-167 (1988)
6. R. Zengerle, S. Kluge, M. Richter, A. Richter, "A bidirectional silicon micropump," *Proc. IEEE Micro Electro Mechanical Systems, MEMS'95* (1995)
7. H. Q. Li, D. C. Roberts, J. L. Steyn, K. T. Turner, J. A. Carretero, O. Yaglioglu, Y.-H. Su, L. Saggere, N. W. Hagood, S. M. Spearing, M. A. Schmidt, R. Mlcak, and K. S. Breuer, "A high frequency high flow rate piezoelectrically driven MEMS micropump," *Proceedings IEEE Solid State Sensors and Actuators Workshop, Hilton Head* (2000).
8. G.-H. Feng, and E. S. Kim, "Piezoelectrically Actuated Dome-Shaped Diaphragm Micro-

pump," *Journal of Microelectromechanical Systems*, **14** (2005)

9. T. Bourouina, A. Bosseboeuf, J.-P. Grandchamp, "Design and Simulation of an electrostatic micropump for drug-delivery applications," *J. Micromech. Microeng.*, **7**, 186-188, (1997)

10. C. Brennen, and H. Winet, "Fluid mechanics of propulsion by cilia and flagella," Ann. Rev. *Fluid Mech.*, **9**, 339-98 (1977)

11. E. M. Purcell, "Life at Low Reynolds Number," *American Journal of Physics*, **45**(1) (1977)

12. J. Gray and G.J. Hancock, "Propulsion of Sea-Urchin Spermatozoa," *J. Exp. Biol.*, **32**, 802-814 (1955)

13. COMSOL AB., *Comsol Multiphysics Modelling Guide* (2005)

14. L. D. Landau, and E. M. Lifshitz, Fluid *Mechanics*, Elsevier Butterworth-Heinemann, Oxford (2005)

15. F. Duarte, R. Gormaz, S. Natesan, "Arbitrary Lagrangian-Eulerian method for Navier-Stokes equations with moving boundaries," *Comput. Methods. Appl. Mech. Engrg.*, **193**, 4819-4836 (2004)

16. A. Winslow, "Numerical solution of the quisilinear Poisson equations in a nonuniform triangle mesh," *J. Comp. Phys.*, **2**, 149-172 (1967)

17. D.F. Katz, "On the propulsion of micro organisms near solid boundaries," *J. Fluid Mech.*, **64**, 33-49 (1974)

18. Sir G. Taylor, "Analysis of the swimming of microscopic organisms," *Proc. Roy. Soc., A*, **209**, 447-61 (1951)

19. A.F. Tabak, S.Yesilyurt, "Analysis of the flow induced by traveling plane-waves on a thin solid-film placed in a channel as a propulsion mechanism for micropumps", *Microfluidics and Nanofluidics* (in preparation).